Mesoscale dynamics and its interaction with coastal upwelling in the northern Gulf of Guinea

Abdoul Karim Thiam, Gael Alory, Isabelle Dadou, Dante Napolitano, Habib Micaël A. Aguedjou, Camille Cardot, Guillaume Morvan, Yves Morel, Julien Jouanno

frontiers | Frontiers in Marine Science

TYPE Original Research
PUBLISHED 27 November 2024
DOI 10.3389/fmars.2024.1500753

OPEN ACCESS

EDITED BY
Marco Bajo,
National Research Council (CNR), Italy

REVIEWED BY
William McKiver,
National Research Council (CNR), Italy
Zhixuan Feng,
East China Normal University, China

*CORRESPONDENCE
Abdoul Karim Thiam
abdoul-karim.thiam@univ-tlse3.fr

RECEIVED 23 September 2024
ACCEPTED 07 November 2024
PUBLISHED 27 November 2024

CITATION
Thiam AK, Alory G, Dadou I, Napolitano D, Aguedjou HMA, Cardot C, Morvan G, Morel Y and Jouanno J (2024) Mesoscale dynamics and its interaction with coastal upwelling in the northern Gulf of Guinea.
Front. Mar. Sci. 11:1500753.
doi: 10.3389/fmars.2024.1500753

Mesoscale dynamics and its interaction with coastal upwelling in the northern Gulf of Guinea

Abdoul Karim Thiam[1]*, Gael Alory[1], Isabelle Dadou[1], Dante Napolitano[1,2], Habib Micaël A. Aguedjou[1], Camille Cardot[1], Guillaume Morvan[1], Yves Morel[1] and Julien Jouanno[1]

[1]Université de Toulouse, LEGOS (CNES/CNRS/IRD/UPS), Toulouse, France, [2]Univ. Brest, LOPS (CNRS/Ifremer/IRD/IUEM), Plouzané, France

Mesoscale dynamics is essential to understanding the physical and biological processes of the coastal ocean regions due to its ability to modulate water properties. However, on the shelf, interactions between eddies, coastal currents, and topography involve complex processes whose observation, understanding, and accurate simulation still pose a major challenge. The purpose of our work is to quantify the mesoscale eddies in the northern Gulf of Guinea, off West Africa (10°W–10°E, 2°N–7°N), and their dynamical interaction with the near-surface ocean particularly in the coastal upwelling that occurs in summer between 2°W and 2°E. We used a regional NEMO model simulation at 1/36° resolution over the 2007–2017 period with daily outputs. A total of 38 cyclonic and 35 anticyclonic eddy trajectories were detected over the 2007–2017 period in July–August–September (JAS), with a mean radius along their trajectories of 95 km and 125 km, respectively. The mean lifetime for cyclones and anticyclones is approximately 1 month with an associated sea-level amplitude between 1 and 2 cm. We then focused on the JAS upwelling period of the year 2016 and found a 73 km radius cyclonic eddy east of Cape Three Points (Ghana) with a lifetime of 1 month which interacted with the coastal upwelling. Indeed, the quasi-stationary eddy dwelled within the coastal upwelling region from mid-July to mid-August 2016. A Lagrangian study shows that the eddy waters come from the coastal upwelling, then mix with warmer offshore waters, and later are transported eastward by the Guinea Current. Using a heat budget analysis, we show that this eddy–coastal upwelling interaction has an impact on sea surface temperature (SST) with a double effect: i) the eddy expands offshore the cold and salty waters (23°C and 35.6) of the coastal upwelling from 14 to 26 July; and ii) from 27 July until its dissipation, the eddy weakens this upwelling by an easterly inflow of warm offshore waters. This study highlights how the eddy–upwelling interaction can modulate the coastal upwelling in the northern Gulf of Guinea.

KEYWORDS

sea surface temperature, Gulf of Guinea, modeling, eddy, coastal upwelling, eddy-upwelling interaction, coast-offshore exchange, Lagrangian simulation

1 Introduction

In the ocean, the mesoscale represents spatial scales from 10 km to a few hundred km. The dynamics at those scales are dominated by quasi-circular structures with a temporal scale of the order of days to months; these so-called mesoscale eddies have properties like polarity (cyclonic or anticyclonic rotation), eddy kinetic energy (EKE), radius, amplitude of the associated sea-level anomaly (SLA), and lifetime, which are in general related to their mechanisms and locations of formation (e.g., Chaigneau et al., 2009; Chelton et al., 2011; Aguedjou et al., 2019, 2021).

The dynamics associated with these mesoscale features play an important role in the ocean's physical and biogeochemical properties. Indeed, these eddies have the ability to trap water masses in their formation regions and transport them through different regions, with their core isolated from surrounding waters. Eddies can propagate over long distances; for instance, between the coastal and the open ocean and when losing coherence can significantly modify the temperature, salinity, and nutrients of local water masses (e.g., Chelton et al., 2011; Hasson et al., 2019).

Locally, near the surface, cyclonic (anticyclonic) eddies are generally associated with negative (positive) SLA that in turn are positively correlated to negative (positive) sea surface temperature (SST) anomalies due to vertical/horizontal advection or mixing. However, some studies show a negative correlation between SST and SLA or even no correlation at all in some cases, e.g., due to interaction with the seasonal cycle of the mixed layer dynamics or air–sea interactions (e.g., Hausmann and Czaja, 2012; Liu et al., 2020; Aguedjou et al., 2021, 2023).

Mesoscale eddies can also have a sea surface salinity (SSS) signature due to vertical/horizontal advection or mixing (the same processes as SST) and also the freshwater discharge of rivers such as the Amazon River or the Congo River (e.g., Hasson et al., 2019; Huang et al., 2021b; Aguedjou et al., 2023). These mesoscale structures can also influence the food chain by fueling primary production through an input of nutrients into the euphotic layer. This phenomenon is more noticeable in oligotrophic regions (e.g., Benitez et al., 2007; McGillicuddy, 2016).

In the global ocean, even if mesoscale eddies can appear anywhere depending on the predominant physical processes, there are areas favorable to the genesis of these structures like the Eastern boundary upwelling systems, the coastal-open ocean transition zone, and frontal zones (e.g., Chaigneau et al., 2009; Chelton et al., 2011). In the tropical Atlantic Ocean (TAO), mesoscale eddies can appear in the Benguela and Canary upwelling systems, also at the western boundary along the North Brazil Current retroflection, and in the western part of the North Equatorial Counter Current (e.g., Johns et al., 1990; Aguedjou et al., 2019). These eddies are mainly generated by barotropic and baroclinic instabilities of the main tropical currents, as well as through mixing and frictional processes along the coast and continental slope, and wind stress in the TAO (Assene et al., 2020; Aguedjou et al., 2019, 2021; Napolitano et al., 2022). Tropical instability vortices due to barotropic and baroclinic instabilities, led by the meridional shear of the zonal currents combined with the wind stress and equatorial upwelling front, appear in the Atlantic equatorial band (Athie and Marin, 2008). In the northern part of the Gulf of Guinea, Djakouré et al. (2014) found on average two eddies per year downstream of the Cape Palmas and Cape Three Points where a seasonal upwelling takes place (Figure 1), which is important for the regional climate and the marine resources of the surrounding countries (Caniaux et al., 2011; Kone´ et al., 2017; Djakouré et al., 2017).

Our study is focused on the northern Gulf of Guinea, defined here as the domain (2°N–7°N; 10°W–10°E) in the TAO. This region (see Figure 1) is characterized by a seasonal variability in SST and by two main currents, namely, the Guinea Current (GC) and the Guinea Under Current (GUC, Figure 1), which are mainly zonal (Herbert et al., 2016; Djakouré et al., 2017). These aforementioned characteristics are highly coupled with a seasonal reversal of the wind known as the West African Monsoon (WAM). In summer, south-easterly winds cross the equator and are then deviated in a northeastward direction (Figure 1) favorable to trigger the northern coastal upwelling through an Ekman offshore transport (Caniaux et al., 2011; Djakouré et al., 2017; Brandt et al. 2023). These south-easterlies converge with the north-easterlies over the African continent between 7°N and 11°N bringing strong precipitations in summer over the northern Gulf of Guinea with the maximums of precipitation identified along the intertropical convergence zone (ITCZ) (see Figure 1).

Two main oceanic seasons can be distinguished in the northern Gulf of Guinea: a relatively cold season linked to a coastal upwelling from July to September and a relatively warm season from October to June (Caniaux et al., 2011; Djakouré et al., 2017). The upwelling, characterized by colder SST (Figure 1), takes place along the Côte d'Ivoire and Ghana coasts eastward of Cape Palmas and Cape Three Points. The mechanisms responsible for the upwelling setting off Côte d'Ivoire (Cape Palmas) differ from the ones off Ghana (Cape Three Points). Indeed, the seasonal upwelling is mainly explained at the regional scale by the wind-driven offshore Ekman transport for the Ghana coastal upwelling, whereas the GC strengthening and detachment from the coast could explain the Côte d'Ivoire upwelling (Colin, 1988; Djakouré et al., 2017). Meanwhile, mesoscale eddies are most often found eastward of the Cape Palmas and Cape Three Points where distinct upwelling cells are identified (Binet, 1997; Djakouré et al., 2014). Aguedjou et al. (2023) reported also a hot spot of SST anomalies associated with eddies near the northern coast of the Gulf of Guinea using satellite data.

The aims of our work are to characterize the mesoscale dynamics related to eddies on the northern coast of the Gulf of Guinea and investigate its possible interaction with coastal upwelling for the SST evolution and eddy water properties. For this purpose, we use a modeling approach with consistent dynamics, thoroughly validated by comparison against available observations.

2 Model, data, and method

2.1 Model

The reference simulation used in our study is based on the Nucleus for European Modeling of the Ocean (NEMO; Madec et al.,

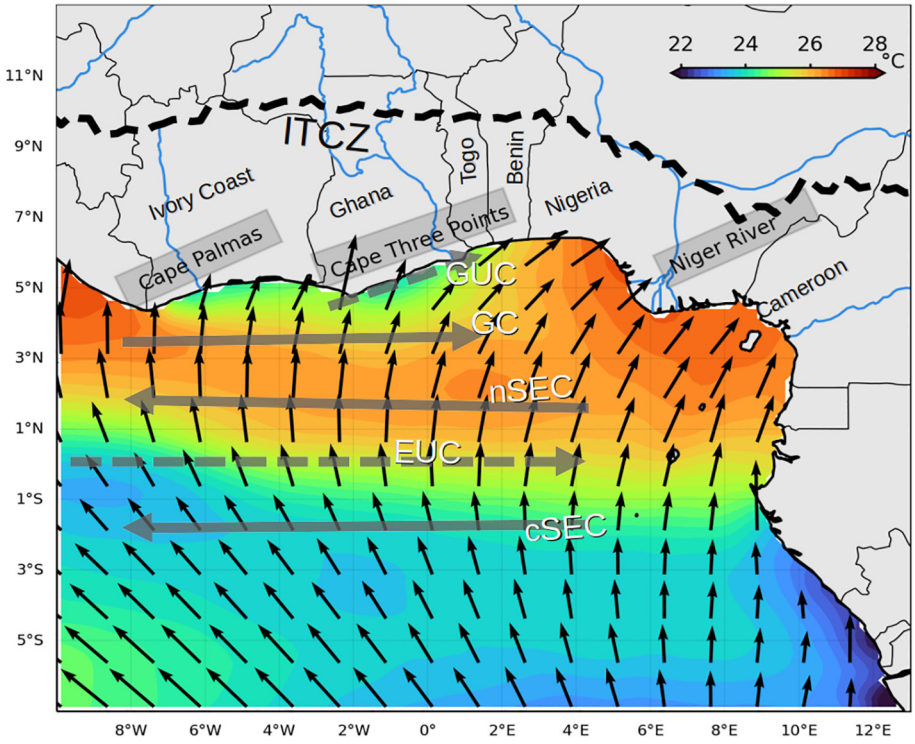

FIGURE 1
Schematic representation of the JAS conditions (averaged over 2007–2017) for SST (shading, from OISST), the surface wind (black arrows, from ASCAT satellite data, and portraying the west African Monsoon), ITCZ positions (black dashed curve), and oceanic currents (gray arrows) in the northern Gulf of Guinea: the Guinea Current (GC), the Guinea Under Current (GUC), the Equatorial Under Current (EUC), and the northern and central branches of the South Equatorial Current (nSEC, cSEC). The ITCZ characterized by the maximum of precipitation using satellite precipitation data [the 3B42 version of the Tropical Rainfall Measuring Mission Multi-satellite Precipitation Analysis (TMPA) distributed by the National Aeronautics and Space Administration (NASA, https://disc.gsfc.nasa.gov/)] is located approximately 9°N in the studied area.

2017) code and covers the Gulf of Guinea (11°W–14°E; 11°S–7°N), with an eddy-resolving 1/36° horizontal resolution and 50 vertical levels; the time step for the simulation is 5 min. Through a bulk formulae based on the NCAR algorithm (Large and Yeager, 2008), the atmospheric heat flux and the wind stress forcing at the ocean surface are based on the Japanese 55-year Reanalysis (1.25° × 1.25° and 3 h), JRA-55 (Kobayashi et al., 2015), and ASCAT satellite data available at a resolution of 1/4°, respectively. Lateral boundary forcing and the initial conditions (temperature, salinity) are from Mercator GLORYS12V1 reanalysis with a 1/12° resolution (Lellouche et al., 2021). The continental freshwater runoff is from the ISBA-CTRIP model (Decharme et al., 2019) except for the Congo River. We use the HYBAM data for the Congo water discharge (https://hybam.obs-mip.fr/data/; Laraque et al., 2020). The runoff temperature is not prescribed in our simulation. The vertical mixing is computed from a turbulent closure scheme using the generic length scale (GLS) formulation, the lateral boundary condition is partial slip (with a coefficient of 0.5), and quadratic friction is applied at the bottom with a roughness of 10^{-6} m. After 2 years of spinup, 11 years (2007–2017) of daily outputs are available. In addition, the daily heat budget terms have been saved for the year 2016, so we will focus on this year for a close analysis of the interaction of mesoscale eddies with sea temperature.

2.2 Data

We used different types of satellite and *in-situ* data for model validation for the summer (JAS) climatological average over the 2007–2017 period.

We used *in-situ* SST data from the Research Program in Physical Oceanography in West Africa (PROPAO) over the period 2008–2012, measured at four stations along the northern coast of the Gulf of Guinea (Sohou et al., 2020).

To assess the ability of the model to reproduce the main surface temperature features in the Gulf of Guinea, we used several monthly temperature datasets: the NOAA 1/4° Optimum Interpolation Sea Surface Temperature (OISST) V2.1 product blending *in-situ* ship and buoy SST with satellite SST derived from the Advanced Very High Resolution Radiometer (AVHRR) (Huang et al., 2021a); the NASA satellite SST product from the moderate resolution imaging spectroradiometer (MODIS) sensor V2019.0 which uses mid-infrared (IR) and thermal IR channels with a resolution of 0.04° (Kilpatrick et al., 2015); the Multi-scale Ultra-high Resolution (MUR) global satellite SST combining infrared and microwave satellite observations with a 0.01° resolution (Chin et al., 2017); the 0.25° Operational Sea Surface Temperature and Sea Ice Analysis V2 (OSTIA) product blending IR satellite and *in-situ* data

(Good et al., 2020); and the World Ocean Atlas climatology (WOA18) based on *in-situ* data (Garcia et al., 2019).

For validating the model's salinity field, we used SSS product from the monthly NASA Soil Moisture Active Passive (SMAP) V5 satellite product with a 0.25° resolution (Fore et al., 2016), SSS from the Soil Moisture Ocean Salinity (SMOS) debiased L3 V07 SSS product with a 0.25° resolution (Boutin et al., 2018), a combined SMOS-SMAP product with higher temporal resolution developed by LOCEAN and available for the Gulf of Guinea (Boutin et al., 2022), and salinity from WOA18. We also used SSS from underway thermosalinographs collected during eight summer cruises or crossings of French research and commercial ships in the Gulf of Guinea between 2000 and 2020 averaged along transects repeated at least three times (Alory et al., 2015; Gaillard et al., 2015).

For validation purposes, we also used a monthly 0.25° climatology of near-surface velocity from satellite-tracked drifting buoys covering the 1979–2019 period (Laurindo et al., 2017). The absolute dynamic topography (ADT) and the geostrophic current used in this work is a 0.25° daily gridded product from Salto/Duacs distributed by the Copernicus Marine Environment Monitoring Service (CMEMS, https://doi.org/10.48670/moi-00148).

2.3 Method

2.3.1 Mesoscale eddy tracking

For the eddy extraction, the algorithm developed by Chaigneau et al. (2009) and Pegliasco et al. (2015), subsequently applied over the TAO by Aguedjou et al. (2019), was used. In this algorithm, the center of an eddy corresponds to a local extremum of the ADT (maximum for anticyclones, minimum for cyclones), while its edge corresponds to the outermost closed ADT contour surrounding the center. In addition to the vortex detection, this algorithm provides information on the vortices properties such as radius, amplitude, EKE, and lifetime as well as their trajectories (for details, see Aguedjou et al., 2019). We only considered eddies that last for at least 7 days and have a minimum median amplitude and radius of 1 cm and 30 km, respectively, all along their trajectory.

For the purpose of our work, this algorithm was applied to the ADT of the altimetry data described above and to the modeled ADT. To compare the two ADT datasets for eddy detection, the modeled ADT has been referenced to the altimetry mean ADT (Equation 1, following Dieng et al., 2019) and also interpolated onto the altimetry grid (1/4°). In Equation 1 $ADT_{model}(t,x,y)$ is the model ADT referenced to the mean altimetry $\overline{ADT_{altimetry}(x,y)}$; SSH_{model} is the model sea surface height. The overbar stands for the time mean over the 2007–2017 period; t, x, and y are the time, longitude, and latitude coordinates, respectively.

$$ADT_{model}(t,x,y) = SSH_{model}(t,x,y) - \overline{SSH_{model}}(x,y) + \overline{ADT_{altimetry}}(x,y) \quad (1)$$

To address the eddy generation mechanism in the context of barotropic/baroclinic instabilities, we used the same Rayleigh (1880) criterion C as in Aguedjou et al. (2019) (their Equation 2)

$$C = \vec{\nabla}(\zeta + f)\cdot\vec{n}\cdot \quad (2)$$

where ζ is the relative vorticity computed from the geostrophic flow, f is the Coriolis parameter, $\vec{n}$ is the unit vector perpendicular to the geostrophic streamlines and obtained by $\vec{n} = \frac{\nabla\psi}{\|\psi\|}$ where $\psi = \left(-\frac{g}{f}\right) * SSH$ is the stream function.

For instabilities to grow, the gradient of the absolute vorticity C should necessarily change sign, thereby eddies located in the area of weak value of C are generated mainly by barotropic instabilities and those in areas of relatively high values of C other processes such as baroclinic instabilities should be invoked.

2.3.2 Lagrangian simulation

In order to study the spatial and temporal evolution of an eddy, we performed Lagrangian particle tracking experiments with daily outputs of the 4D Eulerian modeled fields of velocity, temperature, salinity, and ADT. For this, we performed different virtual float tracking experiments using Parcels v.2.2 (Probably A Really Computationally Efficient Lagrangian Simulator; Delandmeter and Van Sebille, 2019). These experiments were initialized with particles located in an identified vortex at a given date. The initialized particles are advected by the simulated 3D velocity field for a time t, while latitude, longitude, depth, and some physical properties are recorded along their trajectories. The evolution equation for these particles is $X(t+\delta t)$, where X represents the three-dimensional position of the particle at time t. If the time δt is negative, the experiment is said to be backward (upstream) and thus allows us to track where the water trapped in the vortex comes from. If the time δt is positive, the experiment is said to be forward (downstream) and thus allows to follow the fate of the water trapped in the vortex. In order to respect the Courant–Friedrichs–Lewy (CFL) conditions, δt is fixed at 5 min and the equation is time-stepped using the Runge–Kutta fourth-order integration scheme.

2.3.3 Mixed-layer heat budget

The total tendency of ocean temperature within the mixed layer is controlled by different physical processes, expressed in the heat balance (Jouanno et al., 2011) as follows:

$$\underbrace{\frac{\delta\langle T\rangle}{\delta t}}_{\text{Total tendency}} = \underbrace{\underbrace{-\langle u\delta_x T\rangle}_{\text{XAD}} \underbrace{-\langle v\delta_y T\rangle}_{\text{YAD}} \underbrace{-\langle w\delta_z T\rangle}_{\text{ZAD}}}_{\text{Zonal + Meridional + Vertical Advection}} + \underbrace{\langle D_l(T)\rangle}_{\text{Lateral diffusion}} \underbrace{-\frac{1}{h}(K_z\delta_z T)_{z=-h}}_{\text{Vertical diffusion}} + \underbrace{\frac{Q^* + Q_s(1-f_{z=-h})}{\rho\,.\,c_p h}}_{\text{Atmosphere}} \quad (3)$$

with $< X >= \frac{1}{h}\int_{-h}^{0} X dz$ representing the vertical average of a quantity X from the surface to a depth $-h$.

The mixed layer (h) is defined as the depth of the isopycnal representing a 0.03 kg.m^{-3} increment from the density value at 10 m (adapted from Montégut et al., 2004). The same criterion in the northern Gulf of Guinea is used in Alory et al. (2021).

The total sea temperature tendency Equation 3 is controlled by different terms in its RHS, namely, the 3D advection terms, diffusion terms, and the solar and non-solar heat exchanges

between the atmosphere and ocean. For completion, XAD, YAD, and ZAD (units = °C s^{-1}) are, respectively, zonal, meridional, and vertical advection of temperature by the zonal, meridional, and vertical velocity (u, v, w); lateral and vertical diffusion depend, respectively, on lateral and vertical diffusion parameters $D_l(s^{-1})$, K_z $(m^2 . s^{-1})$; the atmospheric component is controlled by the solar radiation heat flux Q_s which is the fraction of solar radiation reaching the base of the mixed layer $f_z = -h$ and non-solar surface heat flux Q^* (sum of longwave radiation, sensible heat and latent heat) at the ocean–atmosphere interface with c_p and ρ being the ocean heat capacity and ocean density, respectively.

All the heat budget terms are computed online during the simulation. Compared to offline computation where the budget terms are calculated from model outputs, online computation allows for a better estimation of these terms (e.g., Ngakala et al., 2023).

In order to quantify the eddy–upwelling influence on the ocean temperature, we evaluated the heat balance inside a box (1.5°W–1°E; 4° N–to the northern coast) that contains the coastal upwelling and the eddy at the box boundary as we will see later. The temperature advection across each boundary delineating the box is estimated by using the method of Lee et al. (2004) to assess external processes controlling the temperature inside the box through advective terms.

To quantify the advective contribution of the mesoscale dynamics, filtering was performed to isolate the part related to the eddy processes from the seasonal processes following the method of Vallis (2017); Napolitano et al. (2019), and Napolitano et al. (2021). The cutoff frequency chosen for the high-frequency filter is 1/30 $days^{-1}$, which is based on the residence time (or lifetime) of the vortex as we will see later. Processes with a frequency higher than 1/30 $days^{-1}$ are considered here as mesoscale processes (or turbulence), and those lower than this frequency are considered other processes such as seasonal processes.

3 Results

3.1 Model validation

To assess the ability of the model to reproduce the main characteristics of the upwelling season in the northern Gulf of Guinea, we compared summer climatology from observations (satellite and *in-situ* data) against the NEMO summer JAS climatology over the 2007–2017 period (Figure 2). We noted the presence of the coastal upwelling, delineated by the 25°C isotherm (Caniaux et al., 2011; Djakouré et al., 2014; Brandt et al., 2023) between 7.2°W and 2°E (Figure 2A), which was enhanced in terms of intensity and amplitude east of Cape Three Points (4.44°N, 2.05° W). This may be related to the fact that there were distinct processes driving the coastal upwelling east of Cape Three Points and Cape Palmas subsequently leading to a westward decrease in the duration and amplitude of the upwelling (Djakouré et al., 2017). Compared to the SST from OISST, the model showed a warm bias of 0.3°C that was noticeable in the area between 2.5°N and 4°N. The upwelling signal was stronger in the model but was narrower concerning the 25°C isotherm extension in OISST. Similar warm biases are shown in Djakouré et al. (2014) and Kone´ et al. (2017) with a regional oceanic modeling system (ROMS/CROCO) configuration performed in the Gulf of Guinea. In the summer season, the

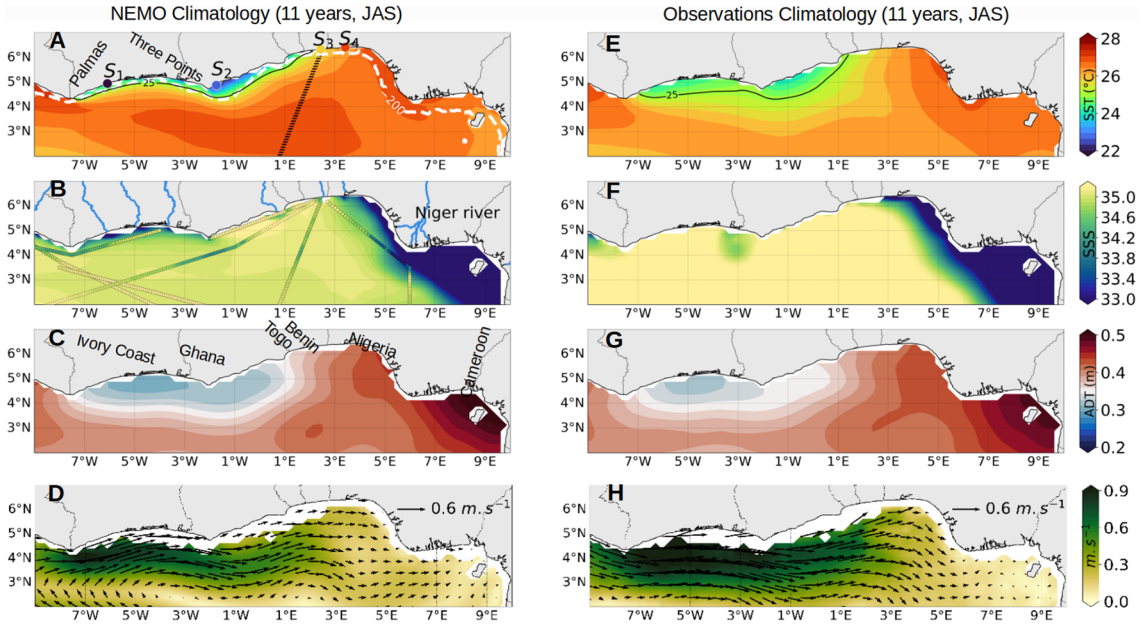

FIGURE 2
Mean summer conditions (July–August–September) on the 2007–2017 period: **(A)** SST, **(B)** SSS, **(C)** ADT, and **(D)** current for the NEMO model on the left side, compared to **(E)** SST from the OISST satellite, **(F)** SSS from the SMAP satellite, **(G)** ADT from CMEMS, and **(H)** current from drifting buoys on the right side. The black isoline in **(A)** is the 25°C isotherm, and the white dash line is the 200-m isobath; the colored dots labeled S1, S2, S3, and S4 are, respectively, *in-situ* mean temperatures from Sassandra (Ivory Coast), Takoradi (Ghana), Cotonou (Benin), and Lagos (Nigeria) stations. Transects in **(B)** are an average from repeated 2000–2020 thermosalinograph measurements.

northern Gulf of Guinea was marked by pronounced convective activity leading to an increase of atmospheric water vapor content then to low-level clouds (like cumulus or stratocumulus) or even cirrus clouds (at higher altitudes) which could cause a cold bias in satellite data if the cloud mask is absent or not well defined (e.g., Marquis et al., 2017). Clouds may partly explain the model warm bias regarding the satellite records. Further inshore, the model SST performed well in comparison with the mean SST of coastal stations S2, S3, and S4. Except for S1, where the model was warmer by 2°C, our model was in general closer to observations than coupled global circulation models, which usually presented biases higher than 2°C (e.g., Toniazzo and Woolnough, 2014; Voldoire et al., 2019).

The model SSS (Figure 2B) displayed saltier waters in the upwelling cell east of Cape Three Points, extending south-eastward. This salty water tongue was also found in Alory et al. (2021). In comparison to SSS from SMAP, the model was on average less salty with a bias of −0.15, but a good agreement was found east of 3°E in the Biafra Bight where relatively fresh water was due to river runoffs and precipitations (Berger et al., 2014; Martin et al., 2021). Note that we identified a radiofrequency interference source (a coastal radar) that was responsible for the SMAP spurious coastal freshening at 3°W (Figure 2F).

Thermosalinograph (TSG)-averaged transects superimposed on model SSS (Figure 2B) were consistent with the latter in the eastern freshwater plume. East of Cape Three Points, in the upwelling cell, high salinity values up to 35 were found in both the TSG and the model. In the salty tongue, between 1°E and 3°E, the model was slightly saltier at latitudes from 3.5°N toward the coast. At the latitudes of the upwelling cell east of Cape Palmas between 7°W and 2.4°W, both the model and TSG showed less salty waters (although their magnitude is slightly different) compared to water salinity eastward of the Cape Three Points between 2°W and 2°E. This difference might be explained either by the fact that in our SST climatology, coastal upwelling is less pronounced east of Cape Palmas than Cape Three Points or by freshwater runoff from the continent. Southward of 4°N, salinity from the TSG and model is comparable although the latter is on average less salty.

We then analyzed the ADT maps from the model and altimetry (Figures 2C, G, respectively). The pattern depicting an eastward positive gradient of the ADT between the coastal upwelling area and the freshwater plume area (Alory et al., 2021) was comparable in both the model and altimetry. There was a good agreement between these two products except for a model underestimation by 2.5 cm east of Cape Three Points (between 2°W and 1°E). Cross-shore ADT gradient is an important feature associated with the GC circulation in the eastern Atlantic Ocean, since the GC is predominantly a geostrophic flow (Djakouré et al., 2017).

The GC is the main eastward current in the northern Gulf of Guinea located between 2°N and the African coast (Figures 2D, H) with a seasonal variability characterized by an intensification and a width extension in summer with values reaching approximately up to 0.6 m s^{-1} and 200 km off the coast, respectively (Herbert et al., 2016; Djakouré et al., 2017). The surface current computed from the model velocity field (Figure 2D) was in accordance with GC features described previously but displayed a low mean bias of −0.04 m s^{-1} with respect to the stronger current observed from drifting buoys (Figure 2H).

To assess the model's vertical structure, we compared vertical sections of temperature and salinity from our NEMO climatology and the WOA18 (Figure 3). The transect in Figure 2A was chosen because it was frequently repeated during PIRATA cruises. Thus, we assumed along this transect that there were enough *in-situ* data for a consistent interpolation in WOA18. We found similar patterns in both the model and WOA18 sections, but temperatures from the model were slightly warmer in the upper 30 m depth, with a large

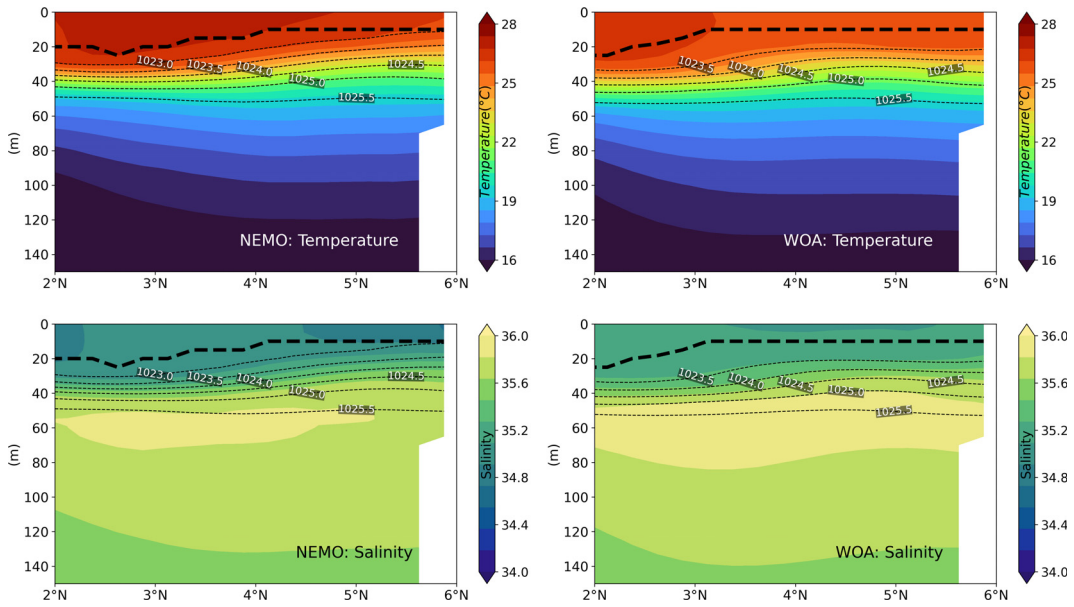

FIGURE 3
Mean summer (2007–2017) cross-shore 0–150 *m* vertical section (black transect in Figure 2A) of temperature and salinity for the model on the left side and for WOA18 on the right side. Thick and thin dashed black lines are mixed layer depth and isopycnals, respectively.

extension of warm water centered between 2°N and 4°N toward the coast. A mixed layer depth (MLD) deepening was noticed between 2°N and 3°N in both the model and WOA18 with a maximum depth of 25 m, whereas toward the coast, the MLD was shallow with 10 to 13 m depth. This MLD shoaling toward the northern coast was mainly explained by a thermocline uplifting associated with the coastal upwelling. Similar patterns of the MLD are found in Berger et al. (2014) and Kone´ et al. (2017). The salinity profile in the model (Figure 3) showed at the surface, between 2.3°N and 4.5°N, values up to 35 which corresponds to SSS in the salty tongue previously identified in Figure 2B. At the subsurface (approximately 60 m depth), a high salinity core (up to 36) was identified in both the model and WOA18 where it was more developed. These subsurface salty waters might be associated with the return branch of the EUC and the GUC (Stramma and Schott, 1999; Herbert et al., 2016).

The observation data mapped here for a model validation purpose were selected among different types of satellite and *in-situ* data, according to a spatial and temporal statistical comparison between the model and these data. This comparison in terms of correlation, standard deviation, mean average bias, and centered root mean square errors is summed up in a Taylor diagram (Figure 4).

Except for the OSTIA product which suggested that the model had a cold bias of −0.09°C, for all the rest, the model showed a warm bias ranging from 0.03°C to 0.63°C depending on whether the OISST, MODIS, MUR, or WOA18 product was used for the SST comparison. MODIS fit better to the model (Figure 4) with the best correlation and nearest standard deviation to the model but showed the warmest model bias. In salinity, for any product among the SMOS, SMAP, blended SMOS-SMAP, and WOA18, the model was less salty with a bias ranging from −0.52 to −0.15, and the model was closest to SMAP. The velocity from the model was 4 cm s^{-1}

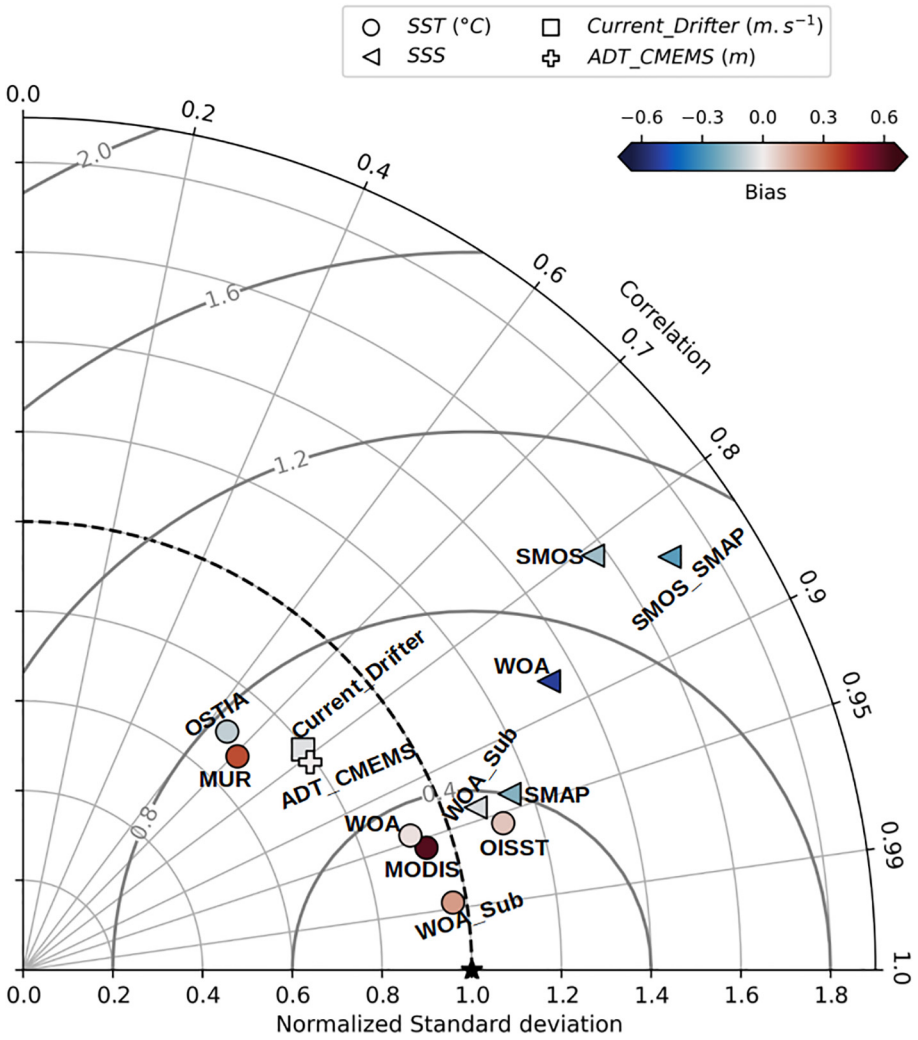

FIGURE 4
Statistical comparison between variables from the model and observation data over the 2007–2017 period in the northern Gulf of Guinea in terms of correlation between the model and observation data, standard deviation, and centered root mean square errors (concentric lines around the black star) of observation data from the model values. The shading colors in the scatter points are biases computed as a model minus the corresponding observation data.

weaker with respect to the drifting buoys' velocity. The ADT model bias was nearly null with a value of 0.2 mm.

Besides these comparisons at the ocean surface between the model and observations, we performed a statistical comparison in the upper 150-m depth along the transect in Figure 3 (WOA Sub in Figure 4). A very good correlation of 0.99 was found between WOA18 and the model temperature with a mean bias of 0.18°C; the salinity field showed also a good correlation of 0.95 and a mean bias of −0.05. These results suggested that the biases in temperature and salinity between the model and WOA18 were mostly found at the surface rather than in the subsurface.

To conclude, the model was able to simulate the main summer features of the northern Gulf of Guinea with some warm and fresh biases that we considered acceptable compared to those of the same order found in the literature within this region. Therefore, our simulation is suitable to investigate mesoscale dynamics in the northern Gulf of Guinea.

3.2 Eddy properties

We now investigated the mesoscale structures (eddies) and their associated properties in the northern Gulf of Guinea over JASO of the 2007–2017 period with daily model outputs and the altimetry data. We included October to take into account eddies formed in September and still persisting through October. Using the algorithm developed by Chaigneau et al. (2009) and Pegliasco et al. (2015) applied on both ADT from the model (assessed from Equation 1) and altimetry, we processed an eddy extraction. We got from it the locations where cyclonic and anticyclonic eddies were born or firstly detected (Figures 5A, E) and the associated properties along the eddy trajectory averaged on a 1° × 1° grid regardless of the polarity (Figures 5B–D, F–H). Only 1° × 1° pixels with an occurrence rate or frequency greater than 2% (≃1 month) were considered for the JASO 2007–2017 period.

We found 38 cyclonic and 35 anticyclonic eddy trajectories from the model against 22 and 34, respectively, for the altimetry (Figures 5A, E). However, both the model and altimetry products agreed on the fact that cyclonic eddies preferentially formed near the coast in the upwelling area eastward of the Cape Palmas (7.43°W, 4.22°N) and Cape Three Points (2.05°W, 4.44°N) (Figures 5A, E), even though less cyclonic eddies were found in the altimetry product due to its limited extension toward the coast. However, anticyclonic eddies were mostly detected along the GC latitudes between 2°N and 4°N and at the vicinity of the Niger River plume east of 2°E, for both the model and altimetry.

The associated radius of the detected eddies could reach more than 120 km (Figures 5B, F) with amplitude up to 2 cm (Figures 5C, G) and last more than 20 days (Figures 5D, H) in both the model and altimetry data.

Statistically, in the northern Gulf of Guinea, 38 cyclonic and 35 anticyclonic eddies were detected over JASO of the 2007–2017

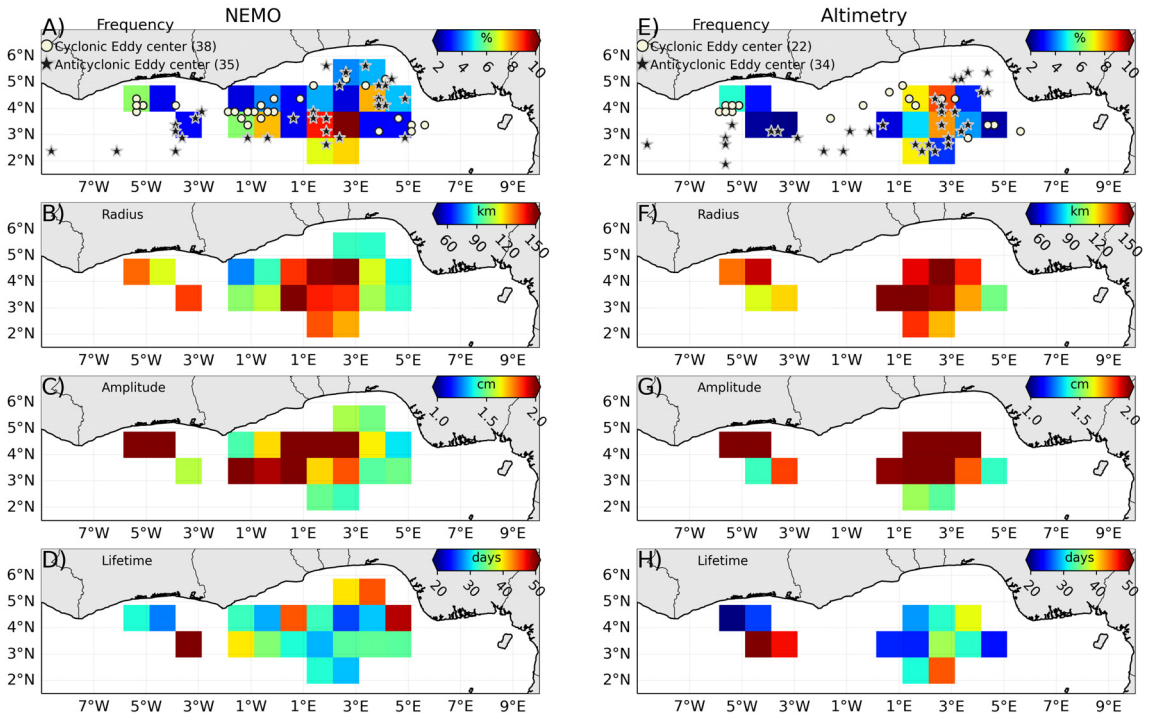

FIGURE 5
Eddy (cyclonic and anticyclonic) birth place and associated mean properties on a 1° × 1° grid in the northern Gulf of Guinea over JAS of the 2007–2017 period: **(A)** the initial position of the eddy trajectory or birth place (filled beige dots for cyclone and filled black stars for anticyclone) and the frequency or occurrence rate (shaded area) for a pixel to be covered by an eddy over July–August–September–October (JASO) of the 2007–2017 period, **(B)** associated radius along their trajectory, **(C)** amplitude, and **(D)** lifetime from the model on the left side and **(E–H)** same as **(A–D)**, respectively, but for altimetry, on the right side.

period from the model, with a mean amplitude of 1.44 cm and 1.03 cm, a mean radius of 95 km and 125 km along their trajectory, and associated mean lifetimes of 21 days and 30 days, respectively.

As expressed in paragraph 2.3.1, to evaluate whether baroclinic or barotropic instabilities are involved in the eddy generation in the northern Gulf of Guinea, we computed the absolute vorticity gradient C (see Equation 2) at locations where and times when eddies are detected for the first time (Figures 6E, F). The spatial distribution of the mean C values over these time steps is shown in Figures 6A–D.

Very similar patterns of the averaged C can be noticed between NEMO and the altimetry (Figures 6A–D), with positive values approximately 3°N and a tendency to negative values northward and southward of 3°N with a zero-crossing approximately 4°N and 2.5°N. This changing sign of the gradient of the absolute vorticity C could enable instabilities to grow according to Charney and Stern (1962) and might explain the high occurrence of eddies formed approximately 4°N and 2.5°N to 3°N (Figures 6A–D).

The associated value of C when eddies form (Figures 6E, F) showed that almost all of the generated anticyclones from both NEMO and altimetry had weak absolute values of C between $-0.5 * 10^{-9}$ and $0.5 * 10^{-9}$ when they form, suggesting that barotropic instabilities could be the main processes responsible for their generation. Cyclonic eddies from altimetry (Figure 6F) were also associated with weak absolute values of C, whereas cyclones from NEMO (Figure 6E) can have relatively high absolute value of C, suggesting that other processes such as baroclinic instabilities could be involved. These discrepancies between NEMO and the altimetry processes that could be related to the formation of cyclonic eddies generally found near the coast may be due to the limited extension of satellite data toward the coast; thus, altimetry can miss out the coastal processes related to friction or baroclinic instabilities. So, this C diagnostic showed a good agreement between the model and the observation for the generation of eddies, except for those formed close to the coast.

Hereafter, we focused on the summer JAS (upwelling season) of the year 2016 in which daily heat budget terms were recorded and studied a possible influence that eddies may have on sea temperature and on heat exchange between the coast and the open ocean.

3.3 Case study of a cyclonic eddy during the summer season

In this section, we focused on a cyclonic mesoscale eddy detected by the algorithm during the JAS upwelling season, east of Cape Three Points. Its signature was associated with a positive relative vorticity at the surface (Figure 7A). This signature was also noticeable in terms of ADT (Figure 7D) by a minimum of ADT enclosed by the cyclone edge and referred to as the eddy center (white dot). One can also notice two large anticyclonic cells (black closed contours with negative vorticity) between 2°N and 4°N and located at longitudes from 7°W to 3°W and between 1°E and 3°E. In this study, we focused on the cyclonic eddy east of Cape Three Points given its proximity to the coastal upwelling and probable interaction with it.

The cyclonic eddy identified on 14 July 2016 was present until 13 August 2016 before dissipating, with a mean radius of 73 km. In the northern hemisphere, a characteristic of cyclonic eddies is that their trajectory is generally oriented to the northwest, but they can

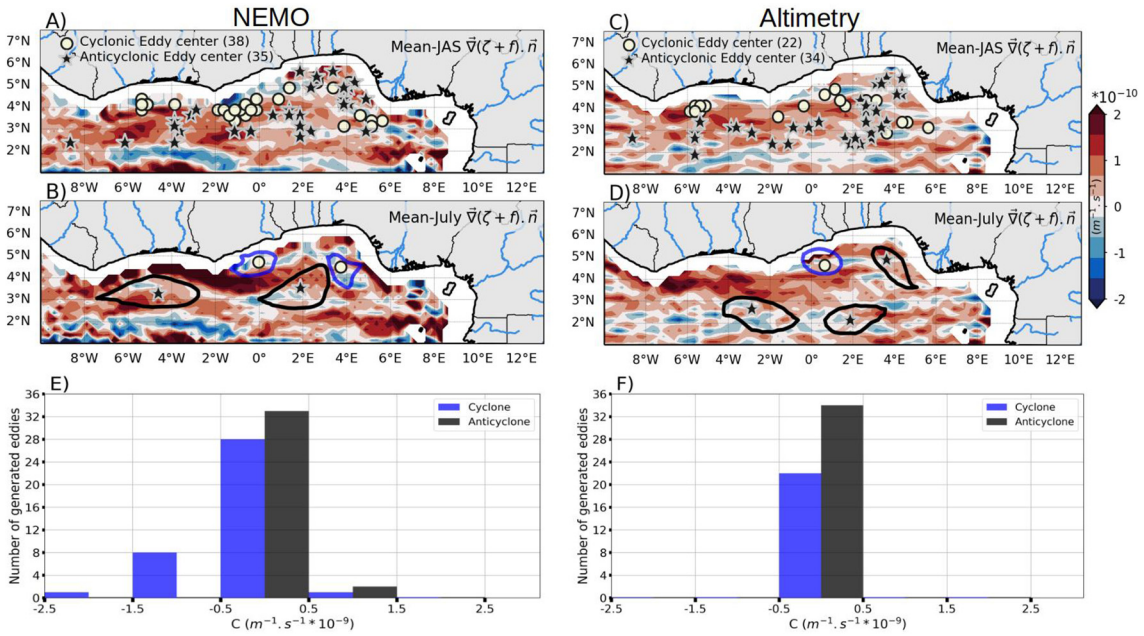

FIGURE 6
Mean **(A, C)** gradient of the absolute vorticity C over time step where eddies are for the first time detected in the JAS 2007–2017 period (shading) from NEMO and altimetry; filled dots and stars are cyclonic and anticyclonic eddy center locations, respectively, at the first time they are detected. **(B, D)** The same as **(A, C)** but for July 2007–2017: closed contours are eddy edges, blue for cyclones and black for anticyclones, and detected in July 2016. The number of generated eddies within different classes of the absolute vorticity gradient C ($m^{-1}\ s^{-1}$) computed the first time the eddy is detected, from **(E)** NEMO and **(F)** from altimetry data. Classes extend from −2.5 to 2.5 ($m^{-1}\ s^{-1} * 10^{-9}$) by an interval of $1 * 10^{-9}\ m^{-1}\ s^{-1}$.

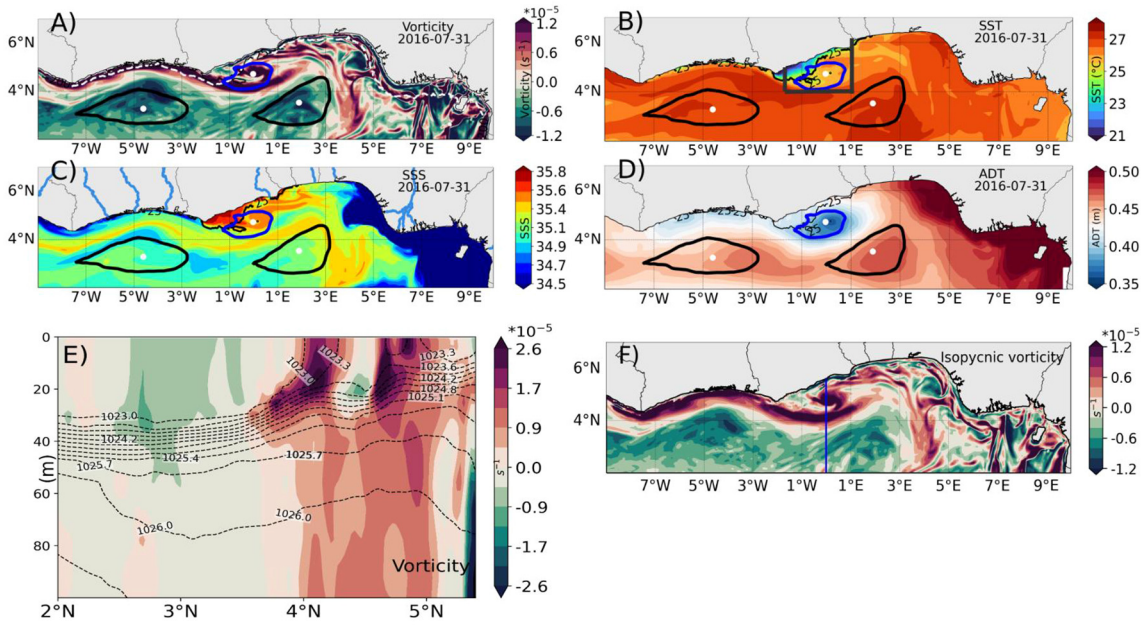

FIGURE 7
Mesoscale diagnostics on 31 July 2016. **(A)** Surface relative vorticity: the white dashed line represents the 200-m isobath, the black 25°C isoline indicates the upwelling threshold, closed contours are eddy edges, blue for cyclone and black for anticyclone, the white dots are eddy centers; **(B)** SST; **(C)** SSS; **(D)** ADT; **(E)** vertical section of the relative vorticity along 0°W [blue line on **(F)**]; **(F)** relative vorticity averaged between the isopycnal 1,025.8 kg/m^3 and the surface level.

deviate from that trajectory when interacting with background currents or topography (Chelton et al., 2011). In our case, the detected cyclone was quasi-stationary between 1.5°W and 1°E and even presented some tendencies to move eastward due to the fact that the eddy was trapped between the shelf break and 4°N, latitude of the GC. This current, as it flowed eastward, prevented the movement of the cyclone to the west, while the shelf topography blocked the movement to the north explaining the trapping between 4°N and the coast.

A signature of the cyclone is that it had cold and salty anomalies that can be seen in SST (Figure 7B) and SSS spatial distribution (Figure 7C). In addition, eastward of the Cape, the surface salty filament associated with the coastal upwelling extended offshore with a tendency to curl counterclockwise around the cyclonic eddy (Figure 7C) following the relative vorticity (Figure 7A). The cyclonic eddy extended from the surface downward to 50 m depth. Its core, depicted by the highest relative vorticity anomaly, was located within the pycnocline, approximately 20 m, and near the coast from 4°N to 5.5°N (Figure 7E). We calculated the relative vorticity of the eddy structure integrated between the 1,025.8-kg/m^3 isopycnal and the surface (Figure 7F). The mean relative vorticity of this layer indicated a positive anomaly associated with the cyclonic dynamics of the vortex between 4°N and the northern coast (Figure 7F).

3.4 Origin and fate of the water within the cyclone

In this section, we studied the water properties within the cyclone, their origin, and fate. For this purpose, we performed two Lagrangian simulations: a backward simulation (Figure 8) and a forward simulation (not shown).

In the backward simulation, 1,071 virtual particles were initially placed within the first 10 m depth in the cyclone within the closed ADT isocontour of 37 cm (black contour in Figure 8 which is the outermost closed contour delineating the cyclone at this date) at the start date of the vortex formation (14 July 2016).

Then, we performed a backtracking of these virtual particles down to 20 days prior to the cyclonic eddy onset. We found that waters trapped in the cyclone came from the west and east sides of Cape Three Points in the upwelling cell and mostly from a depth between 15 and 30 m. Prior to the cyclone formation, these waters presented temperatures often below 22°C. As they moved upward and southward, toward the cyclone, they warmed up to a temperature between 23°C and 25°C within the eddy.

The salinity field also showed that waters coming from the west and east of the Cape had a relatively high salinity over 35.5 that was associated to the upwelling of salty waters, and once trapped in the cyclone, they underwent a decrease in salinity to approximately 35, probably due to mixing with the surrounding fresher surface water. The forward simulation (not shown) indicated a persistent warming and a freshening of the eddy waters while being transported eastward and then southward by the GC.

3.5 Eddy interaction with coastal upwelling

We made a close assessment of the relative displacement of the cyclonic eddy and the upwelling threshold (Figure 9). The upwelling threshold position is defined as the maximum offshore

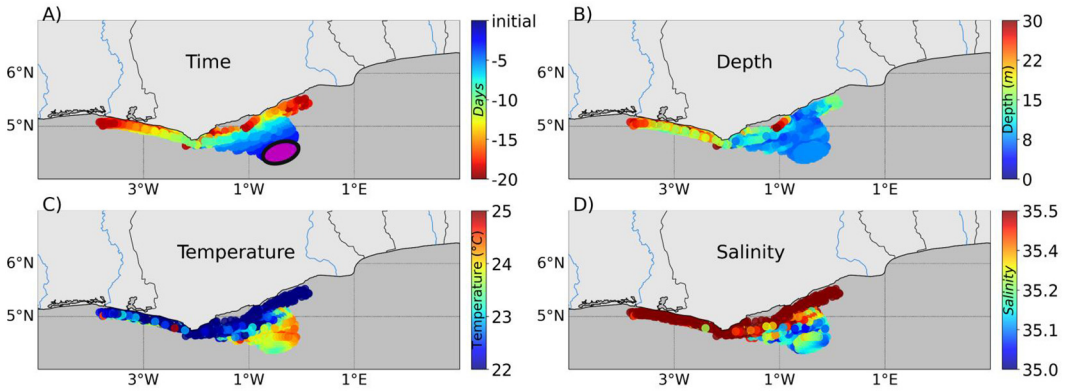

FIGURE 8
Backward Lagrangian simulation of 1,071 virtual particles initialized within the black isocontour on 14 July 2016, the day when the eddy is first detected, and tracked down to 20 days before. Colors represent the evolution of **(A)** time, **(B)** depth, **(C)** temperature, and **(D)** salinity along the particle trajectories.

extension of the 25°C isotherm within the black box represented in Figure 7B.

By July 14 to July 26 (except days ranging from 18 to 21 July where eddy was moving northeastward), the upwelling expanded offshore as the eddy was moving southward and reached its maximum offshore position at 3.7°N (Figures 9A, B). By July 27 until the cyclone started dissipating at approximately August 11, the eddy center was mainly in a southwestward displacement, which is consistent with the upwelling threshold displacement (Figures 9A, B). In a word, eddy displacement is well correlated to the upwelling extension or retraction by 0.64 with a significant level of confidence of 99%.

In the following, we quantified the eddy–upwelling interaction through a mixed-layer temperature budget following Equation 3 within a box containing both eddy and upwelling waters (black box, Figure 7B 1.5°W 1°E; 4°N to the northern coast).

We distinguished on average two main phases in both the mean temperature within the box (Figure 10A) and the total temperature tendency (Figure 10B): one from 17 to 26 July where the main tendency was toward cooling the SST and a second and longer phase from 27 July to 13 August (date of the cyclone dissipation) where the tendency was mostly toward warming of SST; we even noticed some negative trends approximately 3 and 5 August when the eddy and upwelling threshold moved southwestward as we noticed in Figures 9A, B. In the following, these two main phases will be further studied in detail by considering processes associated with advective terms in Equation 3 since the other ones like atmospheric and diffusion processes (Supplementary Figure S1) are less important and neglected compared to advective ones at the 1/30 day^{-1} cutoff frequency that we considered to separate the turbulent from the seasonal or mean signal. The cutoff frequency was determined based on the lifetime of the eddies in the studied area.

The total daily sea temperature tendency inside the box (*Tot*, Figure 10B) was very similar to the total temperature advection (*Tot_adv*) during the cooling phase from 17 to 26 July with a significant correlation coefficient of 0.96. During this phase, the eddy temperature advection (Tot_adv') stood for 98% of the variance of the total temperature advection (*Tot_adv*); therefore, the temperature tendency *Tot* was led by the turbulent (eddy) advection Tot_adv'.

During the warming phase in the upwelling area from 27 July up to the cyclone dissipation on 13 August, the total temperature trend (*Tot*) was significantly correlated to the eddy advective temperature (Tot_adv') by 0.79 which explained 63% of the variance of the total temperature tendency *Tot* (Figure 10B).

During these two phases, we concluded that the internal processes associated with temperature variation within the box were dominated by the eddy advective processes. Hereafter, we assessed the external processes controlling the temperature inside the box following the method of Lee et al. (2004), by assessing the advection of sea temperature through boundaries relative to the spatially averaged temperature inside the box (Figures 10C, D) and providing further details with a spatial–temporal insight of these processes at each boundary (Figure 11). The total external processes through all boundaries (*Total*, Figure 10D) that control the mean temperature inside the box were well correlated to the total turbulent (eddy) external processes $Total'$ by 0.99 with a significance level of confidence of 99%. During the cold phase (from 17 to 26 July), the mean (seasonal) processes in the western and southern boundaries dominated by the GC flow contributed to the warming of the upwelling water in the box, while the turbulent processes associated with the cyclonic eddy were cooling the box (Figures 10C, D). The GC was mainly an eastward flow transporting warmer waters (Figures 2A, D) into the Gulf of Guinea (Herbert et al., 2016) with velocity reaching over 0.6 m s^{-1} in JAS (Djakouré et al., 2014). It was responsible for the warming through the western boundary, as we can notice between 4°N and 4.4°N (Figure 11A). Conversely, the cyclonic eddy partly compensated for this warm inflow into the upwelling cell by turbulent westward circulation that cooled the box (Figure 11B).

Aside from the warming effect of these mean or seasonal processes through the western boundary, one can notice a compensating and persistent cooling through the eastern

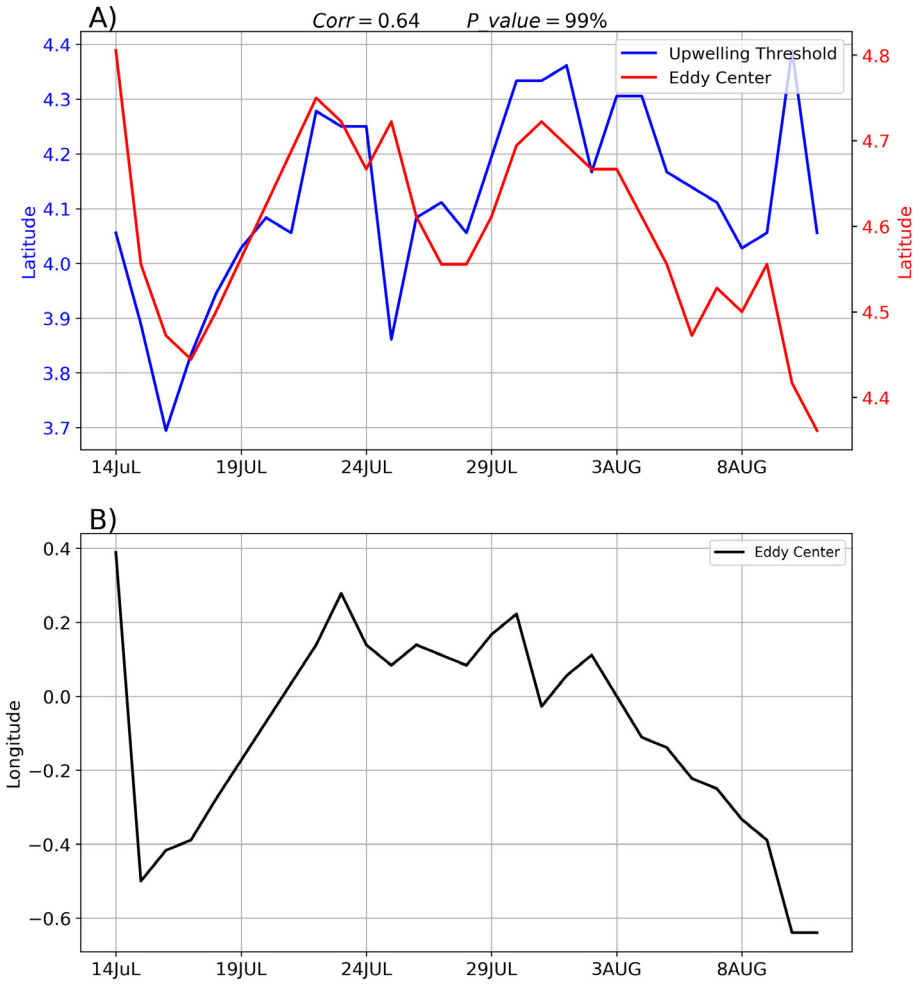

FIGURE 9
Latitudinal **(A)** position of the eddy center and upwelling threshold and longitudinal **(B)** position of the eddy center.

boundary (Figures 10C, 11C), where the cooling effect was also linked to the GC that transported warm waters outside the box through this eastern boundary.

A similar behavior as in the western boundary was also found in the southern boundary. The detachment of the GC from the Cape Three Points fostered cooling in the vicinity of this Cape at the south boundary between 1.5°W and 0.4°W (Figure 11E), but the flow back toward the coast of the GC brought warm offshore water to the upwelling cell area between 0.5°W and the eastern boundary 1°E (Figure 11E). The mean effect of this pattern associated with the seasonal processes related to the GC was a warming through the southern boundary along the eddy lifespan (Figure 10D). In contrast to the GC, the turbulent processes showed on average a cooling tendency in the southern boundary (Figures 10D, 11F) with a period of enhanced cooling between 21 and 26 July (Figures 10D, 11F).

The warming phase from 27 July to 13 August was mainly due to warm turbulent inflow through the eastern boundary (Figure 11D) as the eddy moved westward (Figure 9B). This suggested that eddies often found eastward of Cape Three Points may play a role in the limitation of the upwelling by horizontal advection of warm water from the surrounding Niger River plume.

To underpin the results from the heat budget, we performed a similar analysis with a salinity budget (see Equation 1; Supplementary Figures S2, S3) since salinity is more conservative than temperature. The results from the salinity budget were consistent with those from the heat budget with the two main cold and warm phases clearly depicted in the salinity budget by salty and fresh phases, respectively (Supplementary Figures S2A, B). Furthermore, the total salinity tendency (*Tot*) inside the box was highly correlated to the total advective tendency *Tot_adv* that was in turn led by the turbulent processes, thereby suggesting that the mean salinity tendency inside the box was modulated by the eddy advection (Supplementary Figure S2B). Salinity tendency assessed in each boundary revealed that the warm waters moved in by the GC through the western boundary were on average fresher than those in the upwelling cell which were moved out throughout the eastern boundary by the GC (Supplementary Figures S2C, S3A, C). Meanwhile, the cyclone showed, on average, two patterns: one from 14 to 26 July where the salinity tendency was for a freshening (even some positive tendencies were depicted approximately 19 July) and a second one from 27 July to the eddy dissipation where the salinity tendency was positive (Supplementary Figures S2C, S3B). A

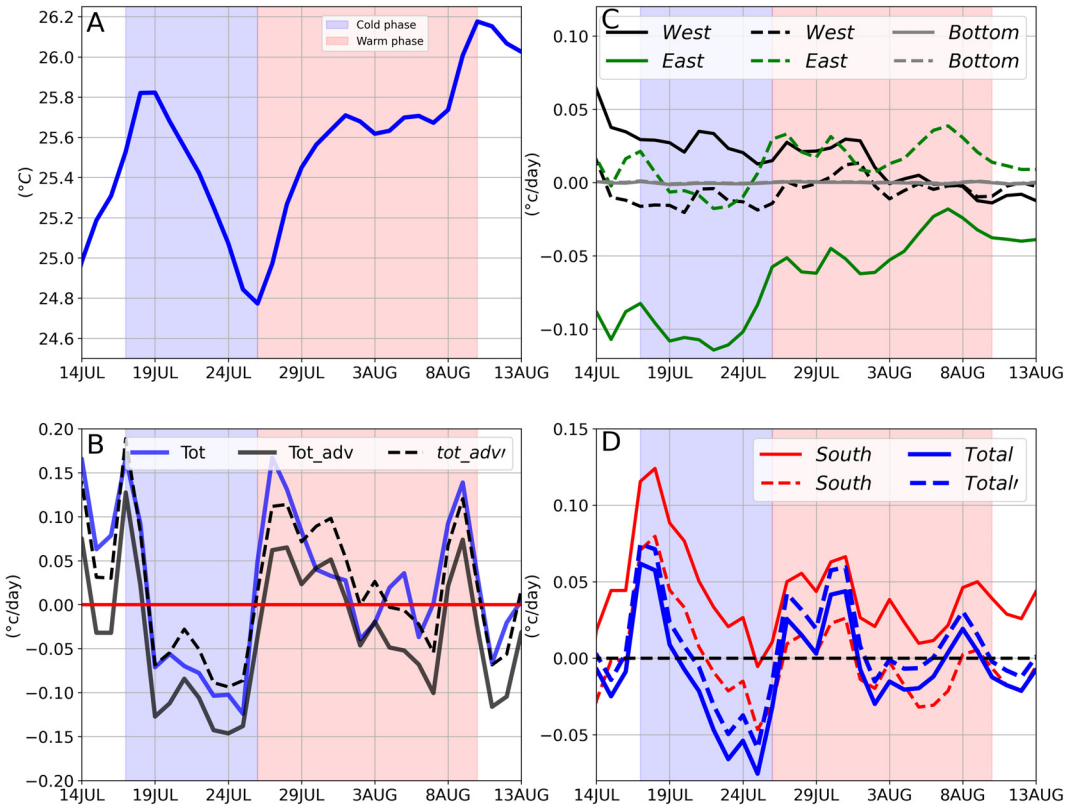

FIGURE 10
Heat budget in the mixed layer within the black box of Figure 2B during the cyclone life period: **(A)** mean temperature within the box in the mixed layer; **(B)** total temperature tendency (Tot), advective temperature tendency (Tot_adv: zonal+meridional+vertical) encompassing both mean (or seasonal) and mesoscale (or turbulent) processes, and eddy (or turbulent) advection of temperature tendency (Tot_adv′); **(C, D)** the advective temperature tendency at each boundary delineating the box (west, east, bottom, and south) and the sum of all boundary advective terms (Total); solid lines include both seasonal and turbulent processes; dashed lines are the mesoscale contribution alone.

freshening through the eastern boundary can be noticed by easterly fresh water inflow (Supplementary Figures S2C, S3D) that was warm (Figure 10C). The cooling at the southern boundary (Figures 10D, 11E, F) due to southward advection was associated with salinity increase, and the coastward advection of warm offshore water was generally associated with a freshening in the box (Supplementary Figures S2D, S3E, F), except east of 0°E before 21 July when warming was associated with salinity increase.

Overall, the results from the salinity budget consistently supported those found in the heat budget.

4 Discussion

The model comparisons with observations show its ability to reproduce the main features characterizing the northern Gulf of Guinea in summer despite some warm and fresh surface biases in which estimations depend on the observation product used as a reference but can reach 0.63°C and −0.52, respectively. The modeling of SST in the Gulf of Guinea is a challenging issue, and the models present warm biases due to ocean modeling or atmospheric forcing. The horizontal resolution for ocean and atmospheric models might be involved as in Earth climate models with warm bias ranging between 2°C and 3°C (Richter, 2015; Toniazzo and Woolnough, 2014). The atmospheric forcing has also some biases; for example, the solar flux is overestimated due to a cloud cover underestimation in the Gulf of Guinea around the ITCZ (Dussin et al., 2016). The wind from the atmospheric model reanalyses does not have the right variability in space and time for a good representation of the wind drop off the coast that can affect coastal upwelling (Fennel et al., 2012; Voldoire et al., 2019; Richter, 2015). So, we decided to use the satellite wind data for the wind forcing of our model configuration over the Gulf of Guinea. This forcing led to a better simulation of the coastal upwelling and river plumes in the Congo region (Ngakala et al., 2024).

Mesoscale cyclonic eddy can be almost detected throughout the year near the northern coast of the Gulf of Guinea with the first peak of detected eddy during the minor upwelling season (February–March) and the second higher peak during the major JAS upwelling season (boxes 1 and 2, Supplementary Figure S4). During the JAS upwelling season in which this study has focused on, under the constraint of the eddy tracking described in Section 2.3.1, at least one cyclonic eddy is detected per year eastward of Cape Palmas (except years 2009, 2013, 2015, and 2017) and eastward of Cape Three Points (except years 2012, 2013, 2014, and 2017) (boxes 1 and 2, Supplementary Figure S5). Cyclonic eddies form either in August or September eastward of Cape Palmas and in July or September eastward of Cape Three Points (Supplementary Figure S5).

10.3389/fmars.2024.1500753

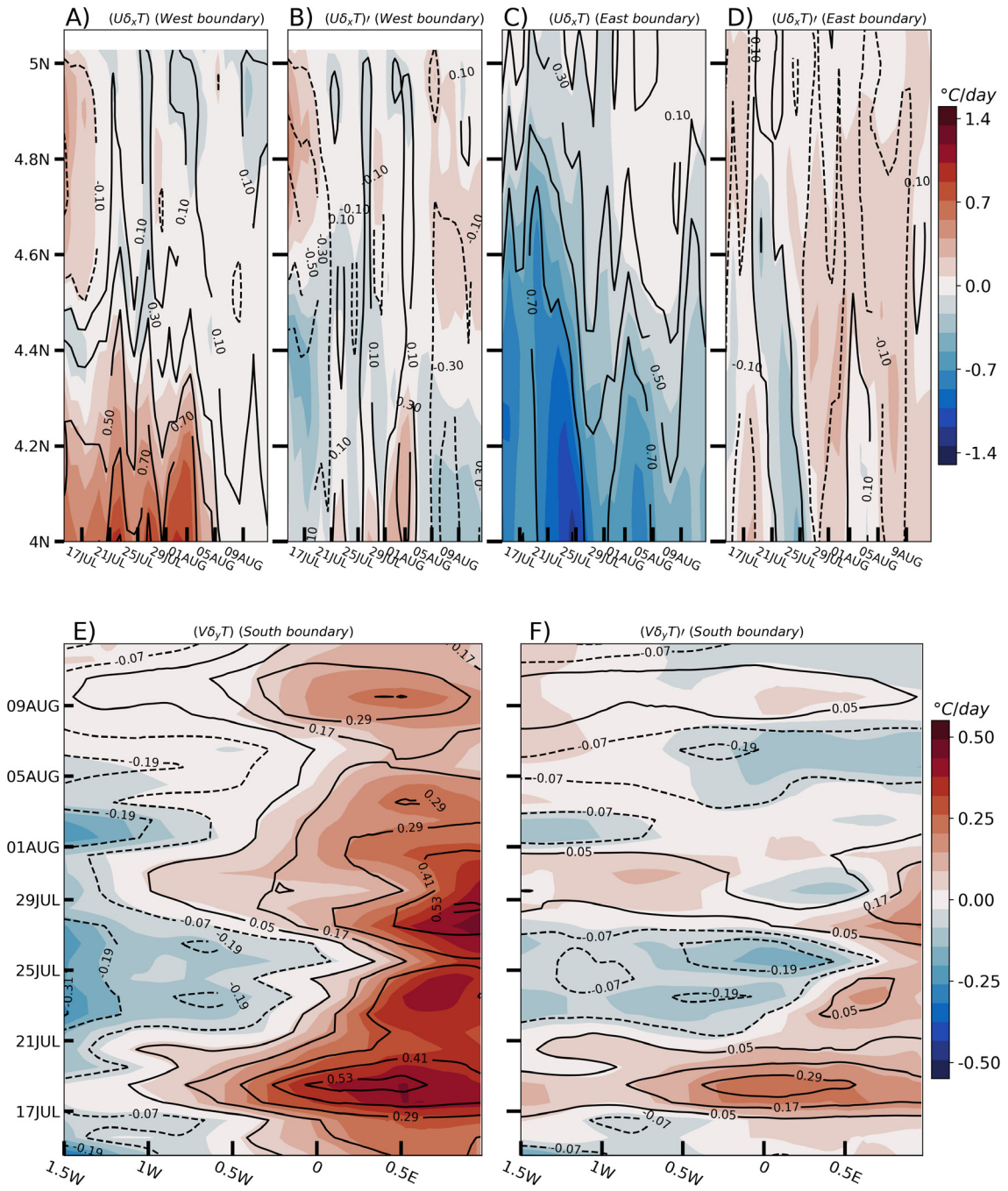

FIGURE 11
Advective heat tendency in the mixed layer at the west boundary for **(A)** seasonal and turbulent (eddy) processes; **(B)** turbulent processes alone; and **(C, D)** and **(E, F)** similar to **(A, B)**, but for east and south boundaries, respectively. Isocontour lines represent the zonal current: **(A, C)** the total zonal current encompassing both mean and turbulent component; **(B, D)** the turbulent component alone; **(E, F)** similar to **(A, C)**, respectively, but for the meridional current. Dashed and solid lines represent negative (westward, southward) and positive (eastward, northward) currents, respectively. Isocontour intervals are 0.2 $m.\ s^{-1}$ and 0.16 $m.\ s^{-1}$ for zonal and meridional currents, respectively.

Different mechanisms can be involved in the eddy generation in the northern Gulf of Guinea during the JAS upwelling season.

Anticyclonic eddies generally forming along the GC latitudes (between 2°N and 3.5°N) are associated with weak gradient values of absolute vorticity C (Figures 6E, F); therefore, barotropic instabilities could lead to their generation. The large-scale GC would be the source of the eddy kinetic energy that triggers instabilities (turbulence) observable through eddies forming at those latitudes (Figures 6A–D). However, cyclonic eddies mostly found near the coast in the upwelling area between 7°W and 2°E (Figure 6A) can be associated with a relatively high absolute value of C (Figure 6E), denoting that processes other than barotropic are

involved. Such processes may include those associated with the wind, outcropping of isopycnals, or baroclinic instabilities. Indeed, upwelling is generally associated with the uplift of deep-level isopycnals that may outcrop at the surface. Such outcropping is systematically associated with positive potential vorticity; therefore, outcropping of isopycnal provides the main reservoir of cyclonic eddy generation (Bretherton, 1966; Morel et al., 2019) and could explain the preference of cyclonic eddy to form in the upwelling cell (Figures 5A, E). Along with outcropping, non-conservative processes such as diapycnal mixing and wind friction (stress) can be invoked. Morel et al. (2006) argue that friction associated with wind stress can act differentially along an isopycnal level and, in this case, triggers systematic negative isopycnal potential vorticity anomalies. The presence of both negative (due to wind stress) and positive (due to outcropping) signs of vorticity anomalies along the isopycnal level could lead to growth of baroclinic/barotropic instabilities according to the Charney and Stern (1962) criterion and further extended to the Rayleigh (1880) criterion for non-parallel sheared currents as seen in Figures 6A–D with *C* values.

The GC interaction with the coastal Capes through frictional effect is also found by Djakouré et al. (2014) to generate an eddy activity.

The Niger River discharge might also, through baroclinic/barotropic instabilities, contribute to the generation of eddies detected east of 2°E (Figures 6A–D).

In the eastern boundary upwelling systems, eddies located along the coastal transition zone can propagate several kilometers offshore with the general nutrient-rich upwelling water; furthermore, the cyclonic eddies are known to generally move in a northwestward direction in the northern hemisphere (Gruber et al., 2011; Chelton et al., 2011). The northern coast of the Gulf of Guinea is in this regard peculiar since it is zonally (west–east) oriented. As a consequence, the transport of water masses associated with eddy dynamics may be blocked by the northern coast and the eastward flow of the GC preventing the eddy to move further northwestward. That is what we found in our case study where the cyclonic eddy was trapped between the GC and the northern shelf and consequently fostered exchanges between water masses from the upwelling cells and those at the vicinity of the GC.

5 Conclusion

The mesoscale dynamics and its possible role in the northern coastal upwelling in the Gulf of Guinea were addressed in this work by using daily outputs from a NEMO ocean model simulation. Validation of the latter was performed with different *in-situ* data and satellite observations in a mean summer (July–August–September) climatological setting covering the 2007–2017 period of the simulation. The model comparisons with observations show its ability to reproduce the main features characterizing the northern Gulf of Guinea in summer.

Using the model ADT field, we performed an eddy extraction over JAS of the 2007–2017 period in the northern Gulf of Guinea. A total of 38 cyclonic and 35 anticyclonic eddies were detected with a mean radius of 95 km and 125 km, a mean lifetime of 21 and 30 days, and associated mean amplitudes along trajectories of 1.44 cm and 1.03 cm, respectively. We found a high occurrence of cyclonic mesoscale structures preferentially forming eastward of Cape Three Points and Cape Palmas, where upwelling occurs in summer. However, anticyclonic eddies are also detected mostly at the Guinea Current at latitudes between 2°N and 4°N and at the vicinity of the Niger River plume.

To investigate the possible influence of the mesoscale dynamics on SST and consequently on the upwelling, we focused on a quasi-stationary mesoscale cyclonic eddy detected just east of Cape Three Points in the summer season JAS of the year 2016 for which heat budget terms were recorded. This cyclonic eddy appeared on 14 July and lasted 1 month with a mean radius of 73 km and was located in the upper surface approximately 20 m depth between the coast and the Guinea Current, in the core of the upwelling cell east of Cape Three Points. Lagrangian simulations show that the waters trapped within the eddy came along the coast from the west and east sides of Cape Three Points, and these waters were previously cold and salty before moving offshore to join the eddy where they mixed with relative warm and less salty waters. The cyclonic eddy shows a double effect on the coastal upwelling: since its formation on 14 July to 26 July, the eddy led to a southward extension of upwelling cold water; from 27 July to its dissipation on August 13, the cyclonic eddy fostered a coastward inflow of warm water which entered in the upwelling area mainly by its eastern boundaries, therefore dampening the formation of the upwelling. These results suggest that the mesoscale eddies frequently found eastward of Cape Three Points and Cape Palmas during the summer may have a prominent role at an intraseasonal scale in the strengthening or weakening of upwelling even if they are not the main causes of the upwelling setting as argued by Djakouré et al. (2014) and Djakouré et al. (2017).

As a perspective, heat budget terms might be recorded for other years; extending our study to these years may underpin or probably find out other features of how mesoscale dynamics may influence the northern Gulf of Guinea upwelling.

Addressing the biochemical properties that may be related to the structure of these eddies would also be a very interesting issue for marine productivity and halieutic resources monitoring since such eddies trapped between the coast and the Guinea Current could foster the spawning and development of some pelagic fishes like *Sardinella aurita*, the most abundant species in the northern Gulf of Guinea.

The observability of these mesoscale eddy structures could also be studied with the new SWOT altimetry mission, taking advantage of its high spatial and temporal resolution enabling an assessment of such structures.

Data availability statement

The original contributions presented in the study are included in the article/Supplementary Material. Further inquiries can be directed to the corresponding author.

Author contributions

AT: Conceptualization, Investigation, Methodology, Software, Validation, Writing – original draft, Writing – review & editing, Data curation. GA: Methodology, Supervision, Validation, Writing – review & editing. ID: Methodology, Project administration, Supervision, Validation, Writing – review & editing. DN: Software, Writing – review & editing. HA: Methodology, Writing – review & editing. CC: Software, Writing – review & editing. GM: Data curation, Writing – review & editing. JJ: Data curation, Writing – review & editing. YM: Supervision, Writing – review & editing.

Funding

The author(s) declare financial support was received for the research, authorship, and/or publication of this article. This work is part of AT's Ph.D. thesis funded by the University of Toulouse (UT3-UPS) (France). This study has benefited from freely available datasets; we thank these diverse platforms, particularly SNO-SSS and PIRATA. We thank the TRIATLAS project funded by the European Union's Horizon 2020 research and innovation program under grant agreement 817578 and the NASA/CNES SWOT-GG project funded by the CNES (TOSCA program) for their various supports. We also thank the (DAAD) Deutscher Akademischer Austauschdienst for their funding. Computing resources are provided by DARI under grant GEN7298.

Acknowledgments

We would like to thank the two reviewers for their constructive comments, which improved our paper.

Conflict of interest

The authors declare that the research was conducted in the absence of any commercial or financial relationships that could be construed as a potential conflict of interest.

Publisher's note

Supplementary material

The Supplementary Material for this article can be found online at: https://www.frontiersin.org/articles/10.3389/fmars.2024.1500753/full#supplementary-material

References

Aguedjou, D. I., Chaigneau, A., Moel, Y., and Alory, G. (2019). Eddies in the tropical atlantic ocean and their seasonal variability. *Geophysical Res. Lett.* 46, 12156–12164. doi: 10.1029/2019GL083925

Aguedjou, C. A., Dadou, I., Morel, Y., Baloïtcha, E., and Da-Allada, C. (2023). Imprint of mesoscale eddies on air-sea interaction in the tropical atlantic ocean. *Remote Sens.* 15, 3087. doi: 10.3390/rs15123087

Aguedjou, H. M. A., Chaigneau, A., Dadou, I., Morel, Y., Pegliasco, C., Da-Allada, C. Y., et al. (2021). What can we learn from observed temperature and salinity isopycnal anomalies at eddy generation sites? application in the tropical atlantic ocean. *J. Geophysical Research: Oceans* 126, e2021JC017630. doi: 10.1029/2021JC017630

Alory, G., Da-Allada, C. Y., Djakouré, S., Dadou, I., Jouanno, J., and Loemba, D. P. (2021). Coastal upwelling limitation by onshore geostrophic flow in the gulf of Guinea around the Niger river plume. *Front. Mar. Sci.* 7. doi: 10.3389/fmars.2020.607216

Alory, G., Delcroix, T., Téchiné, P., Diverrès, D., Varillon, D., Cravatte, S., et al. (2015). The french contribution to the voluntary observing ships network of sea surface salinity. *Deep Sea Res. Part I: Oceanographic Res. Papers* 105, 1–18. doi: 10.1016/j.dsr.2015.08.005

Assene, F., Morel, Y., Delpech, A., Aguedjou, M., Jouanno, J., Cravatte, S., et al. (2020). From mixing to the large scale circulation: How the inverse cascade is involved in the formation of the subsurface currents in the gulf of Guinea. *Fluids* 5, 147. doi: 10.3390/fluids5030147

Athie, G., and Marin, F. (2008). Cross-equatorial structure and temporal modulation of intraseasonal variability at the surface of the tropical atlantic ocean. *J. Geophysical Research: Oceans* 113. doi: 10.1029/2007JC004332

Benitez, C., Bidigare, R. R., Dickey, T. D., Landry, M. R., Leonard, C. L., Brown, S. L., et al. (2007). Mesoscale eddies drive increased silica export in the subtropical pacific ocean. *Science* 316, 1017–1021. doi: 10.1126/science.1136221

Berger, H., Treguier, A. M., Perenne, N., and Talandier, C. (2014). Dynamical contribution to sea surface salinity variations in the eastern gulf of Guinea based on numerical modelling. *Climate dynamics* 43, 3105–3122. doi: 10.1007/s00382-014-2195-4

Binet, D. (1997). Climate and pelagic fisheries in the canary and Guinea currents 1964-1993: The role of trade winds and the southern oscillation. *Oceanolica Acta* 20, 177–190. doi: 10.1029/2020JC016731

Boutin, J., Vergely, J.-L., Marchand, S., d'Amico, F., Hasson, A., Kolodziejczyk, N., et al. (2018). New smos sea surface salinity with reduced systematic errors and improved variability. *Remote Sens. Environ.* 214, 115–134. doi: 10.1016/j.rse.2018.05.022

Boutin, J., Vergely, J., Perrot, X., Olivier, L., Reverdin, X., and Thouvenin-Masson, C. (2022). Smos smap high resolution sss maps in regions of high variability, generated by catds cec. *SEANOE*. doi: 10.17882/90082

Brandt, P., Alory, G., Awo, F. M., Dengler, M., Djakouré, S., Imbol Koungue, R. A., et al. (2023). Physical processes and biological productivity in the upwelling regions of the tropical atlantic. *Ocean Sci.* 19, 581–601. doi: 10.5194/os-19-581-2023

Bretherton, F. P. (1966). Critical layer instability in baroclinic flows. *Q. J. R. Meteorological Soc.* 92, 325–334. doi: 10.1002/qj.49709239302

Caniaux, G., Giordani, H., Redelsperger, J.-L., Guichard, F., Key, E., and Wade, M. (2011). Coupling between the atlantic cold tongue and the west african monsoon in boreal spring and summer. *J. Geophysical Research: Oceans* 116. doi: 10.1029/2010JC006570

Chaigneau, A., Eldin, G., and Dewitte, B. (2009). Eddy activity in the four major upwelling systems from satellite altimetry, (1992–2007). *Prog. Oceanography* 83, 117–123. doi: 10.1016/j.pocean.2009.07

Charney, J. G., and Stern, M. E. (1962). On the stability of internal baroclinic jets in a rotating atmosphere. *J. Atmospheric Sci.* 19, 159–172. doi: 10.1175/1520-0469(1962)019<0159:OTSOIB>2.0.CO;2

Chelton, D. B., Schlax, M. G., and Samelson, R. M. (2011). Global observations of nonlinear mesoscale eddies. *Prog. oceanography* 91, 167–216. doi: 10.1016/j.pocean.2011.01.002

Chin, T., Vazquez-Cuervo, J., and Armstrong, E. (2017). A multi-scale high-resolution analysis of global sea surface temperature. *Remote Sens. Environ.* 200, 154–169. doi: 10.1016/j.rse.2017.07.029

Colin, C. (1988). Coastal upwelling events in front of the ivory-coast during the focal program. *Oceanologica Acta* 11, 125–138.

Decharme, B., Delire, C., Minvielle, M., Colin, J., Vergnes, J.-P., Alias, A., et al. (2019). Recent changes in the isba-ctrip land surface system for use in the cnrm-cm6 climate model and in global off-line hydrological applications. *J. Adv. Modeling Earth Syst.* 11, 1207–1252. doi: 10.1029/2018MS001545

Delandmeter, P., and Van Sebille, E. (2019). The parcels v2. 0 lagrangian framework: new field interpolation schemes. *Geoscientific Model. Dev.* 12, 3571–3584. doi: 10.5194/gmd-12-3571-2019

Dieng, H., Dadou, I., Leger, F., Morel, Y., Jouanno, J., Lyard, F., et al. (2019). Sea level anomalies using altimetry, model and tide gauges along the african coasts in the eastern tropical atlantic ocean: Inter-comparison and temporal variability. *Adv. Space Res.* 68, 534–552. doi: 10.1016/j.asr.2019.10.019

Djakouré, S., Penven, P., Bourlès, B., Kone´, V., and Veitch, J. (2017). Respective roles of the Guinea current and local winds on the coastal upwelling in the northern gulf of Guinea. *J. Phys. Oceanography* 47, 1367–1387. doi: 10.1175/JPO-D-16-0126.1

Djakouré, S., Penven, P., Bourlès, B., Veitch, J., and Kone´, V. (2014). Coastally trapped eddies in the north of the g ulf of g uinea. *J. Geophysical Research: Oceans* 119, 6805–6819. doi: 10.1002/2014JC010243

Dussin, R., Barnier, B., Brodeau, L., and Molines, J. M. (2016). Drakkar forcing set dfs5. *MyOcean Rep*.

Fennel, W., Junker, T., Schmidt, M., and Mohrholz, V. (2012). Response of the benguela upwelling systems to spatial variations in the wind stress. *Continental Shelf Res.* 45, 65–77. doi: 10.1016/j.csr.2012.06.004

Fore, A. G., Yueh, S. H., Tang, W., Stiles, B. W., and Hayashi, A. K. (2016). Combined active/passive retrievals of ocean vector wind and sea surface salinity with smap. *IEEE Trans. Geosci. Remote Sens.* 54, 7396–7404. doi: 10.1109/TGRS.2016.2601486

Gaillard, F., Diverres, D., Jacquin, S., Gouriou, Y., Grelet, J., Le Menn, M., et al. (2015). Sea surface temperature and salinity from french research vessels 2001–2013. *Sci. Data* 2, 1–9. doi: 10.1038/sdata.2015.54

Garcia, H., Boyer, T., Baranova, O., Locarnini, R., Mishonov, A., Grodsky, A., et al. (2019). World ocean atlas 2018: Product documentation. *A. Mishonov Tech. Editor*. doi: 10.13140/RG.2.2.34758.01602

Good, S., Fiedler, E., Mao, C., Martin, M. J., Maycock, A., Reid, R., et al. (2020). The current configuration of the ostia system for operational production of foundation sea surface temperature and ice concentration analyses. *Remote Sens.* 12, 720. doi: 10.3390/rs12040720

Gruber, N., Lachkar, Z., Frenzel, H., Marchesiello, P., Münnich, M., McWilliams, J. C., et al. (2011). Eddy-induced reduction of biological production in eastern boundary upwelling systems. *Nat. Geosci.* 4, 787–792. doi: 10.1038/NGEO1273

Hasson, A., Farrar, J. T., Boutin, J., Bingham, F., and Lee, T. (2019). Intraseasonal variability of surface salinity in the eastern tropical pacific associated with mesoscale eddies. *J. Geophysical Research: Oceans* 124, 2861–2875. doi: 10.1029/2018JC014175

Hausmann, U., and Czaja, A. (2012). The observed signature of mesoscale eddies in sea surface temperature and the associated heat transport. *Deep Sea Res. Part I: Oceanographic Res. Papers* 70, 60–72. doi: 10.1016/j.dsr.2012.08.005

Herbert, G., Bourlès, B., Penven, P., and Grelet, J. (2016). New insights on the upper layer circulation north of the g ulf of g uinea. *J. Geophysical Research: Oceans* 121, 6793–6815. doi: 10.1002/2016JC011959

Huang, L., Liu, C., Banzon, V., Freeman, E., Graham, G., Hankins, B., et al. (2021a). Improvements of the daily optimum interpolation sea surface temperature (doisst) version 2.1. *J. Climate* 34, 2923–2939. doi: 10.1175/JCLI-D-20-0166.s1

Huang, M., Liang, X., Zhu, Y., Liu, Y., and Weisberg, R. H. (2021b). Eddies connect the tropical atlantic ocean and the gulf of Mexico. *Geophysical Res. Lett.* 48, e2020GL091277. doi: 10.1029/2020GL091277

Johns, W. E., Lee, T. N., Schott, F. A., Zantopp, R. J., and Evans, R. H. (1990). The north Brazil current retroflection: Seasonal structure and eddy variability. *J. Geophysical Research: Oceans* 95, 22103–22120. doi: 10.1029/JC095iC12p22103

Jouanno, J., Marin, F., Du Penhoat, Y., Sheinbaum, J., and Molines, J.-M. (2011). Seasonal heat balance in the upper 100 m of the equatorial atlantic ocean. *J. Geophysical Research: Oceans* 116. doi: 10.1029/2010JC006912

Kilpatrick, K. A., Podestá, G., Walsh, S., Williams, E., Halliwell, V., Szczodrak, M., et al. (2015). A decade of sea surface temperature from modis. *Remote Sens. Environ.* 165, 27–41. doi: 10.1016/j.rse.2015.04.023

Kobayashi, S., Ota, Y., Harada, Y., Ebita, A., Moriya, M., Onoda, H., et al. (2015). The jra-55 reanalysis: General specifications and basic characteristics. *J. Meteorological Soc. Japan. Ser. II* 93, 5–48. doi: 10.2151/jmsj.2015-001

Kone´, V., Lett, C., Penven, P., Bourlès, B., and Djakouré, S. (2017). A biophysical model of s. aurita early life history in the northern gulf of Guinea. *Prog. oceanography* 151, 83–96. doi: 10.1016/j.pocean.2016.10.008

Laraque, A., Moukandi N'kaya, G. D., Orange, D., Tshimanga, R., Tshitenge, J. M., Mahé, G., et al. (2020). Recent budget of hydroclimatology and hydrosedimentology of the congo river in central africa. *Water* 12, 2613. doi: 10.3390/w12092613

Large, W., and Yeager, S. (2008). The global climatology of an interannually varying air–sea flux data set. *Climate dynamics* 33, 341–364. doi: 10.1007/s00382-008-0441-3

Laurindo, L., Mariano, A., and Lumpkin, R. (2017). An improved near-surface velocity climatology for the global ocean from drifter observations. *Deep Sea Res. Part I: Oceanographic Res. Papers* 124, 73–92. doi: 10.1016/j.dsr.2017.04.009

Lee, T., Fukumori, I., and Tang, B. (2004). Temperature advection: Internal versus external processes. *J. Phys. Oceanography* 34, 1936–1944. doi: 10.1175/1520-0485(2004)034%3C1936:TAIVEP%3E2.0.CO;2

Lellouche, J.-M., Eric, G., Romain, B.-B., Gilles, G., Angélique, M., Marie, D., et al. (2021). The copernicus global 1/12 oceanic and sea ice glorys12 reanalysis. *Front. Earth Sci.* 9. doi: 10.3389/feart.2021.698876

Liu, Y., Yu, L., and Chen, G. (2020). Characterization of sea surface temperature and air-sea heat flux anomalies associated with mesoscale eddies in the south China sea. *J. Geophysical Research: Oceans* 125, e2019JC015470. doi: 10.1029/2019JC015470

Madec, G., Bourdallé-Badie, R., Bouttier, P.-A., Bricaud, C., Bruciaferri, D., Calvert, D., et al. (2017). Nemo ocean engine.

Marquis, J. W., Bogdanoff, A. S., Campbell, J. R., Cummings, J. A., Westphal, D. L., Smith, N. J., et al. (2017). Estimating infrared radiometric satellite sea surface temperature retrieval cold biases in the tropics due to unscreened optically thin cirrus clouds. *J. Atmospheric Oceanic Technol.* 34, 355–373. doi: 10.1175/JTECH-D-15-0226.1

Martin, A., Guimbard, S., Koehler, J., Akhil, V., Vialard, J., Houdegnonto, O., et al. (2021). Climate change initiative+ (cci+) phase 1 sea surface salinity: Product validation and intercomparison report (pvir).

McGillicuddy, DJ. Jr (2016). Mechanisms of physical-biological-biogeochemical interaction at the oceanic mesoscale. *Annu. Rev. Mar. Sci.* 8, 125–159. doi: 10.1146/annurev-marine-010814-015606

Montégut, C., Madec, G., Fischer, A. S., Lazar, A., and Iudicone, D. (2004). Mixed layer depth over the global ocean: An examination of profile data and a profile-based climatology. *J. Geophysical Research: Oceans* 109. doi: 10.1029/2004JC002378

Morel, Y. G., Darr, D. S., and Talandier, C. (2006). Possible sources driving the potential vorticity structure and long-wave instability of coastal upwelling and downwelling currents. *J. Phys. oceanography* 36, 875–896. doi: 10.1175/JPO2899.1

Morel, Y., Gula, J., and Ponte, A. (2019). Potential vorticity diagnostics based on balances between volume integral and boundary conditions. *Ocean Model.* 138, 23–35. doi: 10.1016/j.ocemod.2019.04.004

Napolitano, D., Alory, G., Dadou, I., Morel, Y., Jouanno, J., and Morvan, G. (2022). Influence of the gulf of Guinea islands on the atlantic equatorial undercurrent circulation. *J. Geophysical Research: Oceans* 127, e2021JC017999. doi: 10.1029/2021JC017999

Napolitano, D. C., da Silveira, I. C., Rocha, C. B., Flierl, G. R., Calil, P. H., and Martins, R. P. (2019). On the steadiness and instability of the intermediate western boundary current between 24 and 18 s. *J. Phys. Oceanography* 49, 3127–3143. doi: 10.1175/JPO-D-19-0011.1

Napolitano, D. C., da Silveira, I., Tandon, A., and Calil, P. H. (2021). Submesoscale phenomena due to the Brazil current crossing of the vitória-trindade ridge. *J. Geophysical Research: Oceans* 126, e2020JC016731. doi: 10.1029/2020JC016731

Ngakala, R. D., Alory, G., Da-Allada, C. Y., Kom, O. E., Jouanno, J., Rath, W., et al. (2023). Joint observation–model mixed-layer heat and salt budgets in the eastern tropical atlantic. *Ocean Sci.* 19, 535–558. doi: 10.5194/os-19-535-2023

Ngakala, R., Alory, G., Y. Casimir, D.-A., Dadou, I., Cardot, C., Morvan, G., et al. (2024). Seasonal mixed-layer temperature in the congolese upwelling system (cus). doi: 10.22541/essoar.169724942.21688528/v1

Pegliasco, C., Chaigneau, A., and Morrow, R. (2015). Main eddy vertical structures observed in the four major eastern boundary upwelling systems. *J. Geophysical Research: Oceans* 120, 6008–6033. doi: 10.1002/2015JC010950

Rayleigh, L. (1880). On the stability, or instability, of certain fluid motions. *Proc. London Math. Soc.* 1, 57–72.

Richter, I. (2015). Climate model biases in the eastern tropical oceans: Causes, impacts and ways forward. *Wiley Interdiscip. Reviews: Climate Change* 6, 345–358. doi: 10.1002/wcc.338

Sohou, Z., Kone´, V., Da-Allada, Y., Djakouré, S., Bourlès, B., Racape, V., et al. (2020). Seasonal and inter-annual onset sea surface temperature variability along the northern coast of the gulf of Guinea. *Regional Stud. Mar. Sci.* 35, 101129. doi: 10.1016/j.rsma.2020.101129

Stramma, L., and Schott, F. (1999). The mean flow field of the tropical atlantic ocean. *Deep Sea Res. Part II: Topical Stud. Oceanography* 46, 279–303. doi: 10.1016/S0967-0645(98)00109-X

Toniazzo, T., and Woolnough, S. (2014). Development of warm sst errors in the southern tropical atlantic in cmip5 decadal hindcasts. *Climate dynamics* 43, 2889–2913. doi: 10.1007/s00382-013-1691-2

Vallis, G. K. (2017). *Atmospheric and oceanic fluid dynamics* (United Kingdom: Cambridge University Press).

Voldoire, A., Exarchou, E., Sanchez-Gomez, E., Demissie, T., Deppenmeier, A.-L., Frauen, C., et al. (2019). Role of wind stress in driving sst biases in the tropical atlantic. *Climate Dynamics* 53, 3481–3504. doi: 10.1007/s00382-019-04717-0